Available online at www.sciencedirect.com
ScienceDirect
Proceedings of the Combustion Institute 33 (2011) 2255–2263
Proceedings of the Combustion Institute
www.elsevier.com/locate/proci

Clustering and combustion of dilute aluminum particle clouds in a post-detonation flow field

K. Balakrishnan, S. Ukai, S. Menon *

School of Aerospace Engineering, Georgia Institute of Technology, 270 Ferst Drive, Atlanta, GA 30332-0150, USA

Available online 24 September 2010

Abstract

A hybrid two-phase numerical methodology is used to investigate the flow-field subsequent to the detonation of a spherical charge of TNT with an ambient distribution of a dilute cloud of aluminum particles. The interaction of the particle cloud with the contact surface results in Rayleigh–Taylor instability, which grows in time and gives rise to a mixing layer where the detonation products mix with the air and afterburn. At early times, the ambient particles get engulfed into the detonation products and ignite. Subsequently, they catch up with the Rayleigh–Taylor structures, and the vortex rings around the hydrodynamic structures cause transverse dispersion that results in the clustering of particles. Then, the particles leave the mixing layer and quench, yet preserve their hydrodynamic foot print. Preferential heating and combustion of particles occurs due to clustering. A higher initial mass loading in the ambient cloud results in larger clusters due to stronger/larger vortex rings around the hydrodynamic structures. A larger particle size results in the formation of fewer and degenerate clusters when the initial width of the cloud is larger. A theoretical model is used to predict the bubble amplitudes, and are in good accordance with the simulation results. Overall, this study has provided some useful insights on the explosive dispersal of dilute aluminum particle clouds and the gas dynamics of the flow field in the mixing layer.
© 2010 The Combustion Institute. Published by Elsevier Inc. All rights reserved.

Keywords: Explosive; Blast wave; Ignition; Clustering; Hydrodynamic instability

1. Introduction

The study of the interaction of a high explosive generated flow field with reactive solid particles has been undertaken recently [1–3], and is a field of research gaining interest. Computational simulations have shown that hydrodynamic instabilities such as Rayleigh–Taylor [4] and Richtmyer–Meshkov [5] occur in the flow field behind blast waves [6–8], thereby resulting in a turbulent mixing layer where the inner detonation products mix with the outer air and burn, accompanied by an exothermic energy release. Subsequent to the detonation, as the contact surface overtakes the particles and engulfs them into the detonation products, the particles introduce perturbations on the contact surface due to momentum and energy absorption, which subsequently grow into Rayleigh–Taylor instability [4]. Then, the particles pick up significant momentum and energy from the gas, are set into motion, and catch up with the hydrodynamic structures.

The hydrodynamic instabilities on the contact surface grow as bubbles of lighter fluid rising into the heavier fluid, and spikes of heavier fluid falling

* Corresponding author. Fax: +1 404 894 2760.
E-mail address: suresh.menon@aerospace.gatech.edu (S. Menon).

1540-7489/$ - see front matter © 2010 The Combustion Institute. Published by Elsevier Inc. All rights reserved.
doi:10.1016/j.proci.2010.07.064

into the lighter fluid. Subsequently, a bubble competition [9–11] ensues in which contiguous hydrodynamic structures of different wavelengths can interact and merge, giving rise to a mixing layer (ML) where afterburn occurs between the detonation products and air [6–8]. Concurrent to these phenomena, the inward moving rarefaction wave over-expands the flow near the core of the charge—this creates a secondary shock (SS) that implodes, reflects from the origin, then explodes and interacts with the hydrodynamic structures in the ML, giving rise to a Richtmyer–Meshkov instability [5]. Here, vorticity is created by the baroclinic mechanism, which further enhances the mixing process and later results in a turbulent ML.

The particles can either get completely engulfed into the detonation products, or exist in the ML, or penetrate into the outside air—allowing for three possibilities for their existence at a given time instant. As the particles disperse outwards, they interact with the vortex rings around the hydrodynamic instabilities in the ML, causing them to cluster, as we will show in this paper. In [7], we explored aluminum particles of 10 μm radius and higher, and did not observe any transverse dispersion of the particles due to these larger particle sizes having slower response time scales. In this paper, the focus is on 5 and 10 μm particle radius clouds, as these smaller particles have faster response time scales, which can significantly affect their dispersion characteristics as they can be influenced by the fluid dynamic time scales of relevance in the ML; in particular, the vortex rings around the Rayleigh–Taylor structures play a prominent role in particle ignition and dispersion as we will show in this study.

The main objectives of this paper are to understand the interaction of an ambient cloud of aluminum particles with the detonation products of a TNT explosion, with particular attention on the effects of three-dimensional physics such as hydrodynamic instabilities on the dispersion and combustion of aluminum particle clouds in post-detonation flow fields. The parameters of interest in the study have applications in the investigation of Shock Dispersed Fuel (SDF) charges [2] as well as aluminized explosives. While this study considers aluminum particles due to recent interest in its burning under shocked/detonation conditions [12,13], the same approach can be extended to magnesium and zirconium as well—other metals widely used in explosives. The ignition, combustion and clustering effects of the particle cloud are studied in detail and explained. This paper is organized as follows: in Section 2, we present the governing equations and the numerical methodology; in Section 3, the results from the current study are reported and the involved physics elucidated; finally, in Section 4, the conclusions drawn from this research effort are presented.

2. Method of study

2.1. Gas-phase

We solve the compressible, unsteady, multiphase gas-phase equations using a finite-volume method [14–16], not presented here for brevity. Whereas the large scales are resolved, an eddy viscosity (ν_t) closure is used to model the small scales [14–16], summarized below:

$$\nu_t = C_\nu \Delta \sqrt{k^{sgs}}; \quad \Delta = (\Delta x \Delta y \Delta z)^{1/3}, \tag{1}$$

where k^{sgs} denotes the sub-grid kinetic energy and $\Delta x, \Delta y$ and Δz are the local grid spacing in the x-, y- and z-directions, respectively. k^{sgs} is obtained by solving a one-equation transport [14–16], with the production ($P_{k^{sgs}}$) and dissipation ($D_{k^{sgs}}$) of k^{sgs} obtained as $P_{k^{sgs}} = \frac{\partial}{\partial x_i}(\bar{\rho}\nu_t \frac{\partial k^{sgs}}{\partial x_i})$; $D_{k^{sgs}} = C_\epsilon \bar{\rho} \frac{(k^{sgs})^{1.5}}{\Delta}$. Here, $\bar{\rho}$ is the filtered gas density; C_ν and C_ϵ are constants [16]. Detonation profiles based on the Gas-Interpolated-solid Stewart–Prasad–Asay (GISPA) method [17] are computed from a 1D simulation that assumes finite reaction rate, and are extrapolated to a 3D sector grid [6,7]. In the afterburning phase, the chemical reaction rate, $\dot{\omega}_k$, is assumed to be infinitely fast and a six-step chemistry is used [7]. For thermodynamic closure, we employ the Noble–Abel equation of state [7], which is typically used for post-detonation behavior of explosives.

A hybrid approach is employed that uses the MUSCL shock-capturing scheme with the HLLC/E Riemann solver [18] in regions dominated by discontinuities, and a central scheme in relatively smooth regions of turbulence [14]. Overall, the scheme is second-order accurate in both time and space. Several canonical studies have been carried out recently to verify the simulation strategy and the numerical approach used in the current hydrocode [7,14,15] with success.

2.2. Solid phase

The Lagrangian tracking approach is used to compute the particle position and velocity vectors from the forces acting on a particle; these kinematic equations are not summarized here for brevity, and can be found in [7,16]. The heat transfer between the two-phases is estimated assuming convection and radiation, and is used to obtain the solid particle temperature. The aluminum evaporation rate is obtained from the widely used empirical quasi-steady evaporation law following other studies [7,19]:

$$\frac{dr_p}{dt} = -\frac{r_p}{t_b}\left(1 + 0.276\sqrt{Re}\right), \tag{2}$$

where r_p denotes the particle radius, t_b is the burning time, and Re is the Reynolds number ($Re = \frac{\bar{\rho}|\tilde{u}_g - u_p|2r_p}{\mu}$; $\tilde{u}_g$ is the filtered gas velocity, u_p is the particle velocity and μ is the viscosity of

the gas). Two regimes of aluminum combustion exist: diffusion and kinetic [12,13], and appropriate burn times need to be used. We use the evaporation law as specified in Eq. (2) with the burn time data from [12], and assume the ignition temperature of the aluminum particles to be 1000 K [7].

A fourth order Runge–Kutta scheme is used to solve the solid phase governing equations to obtain the solid particle position vector, velocity vector, temperature and radius. The coupling terms that are source terms to the gas-phase are computed as a summation, accounting for interphase mass, momentum and energy transfer, and are summarized in [7,16].

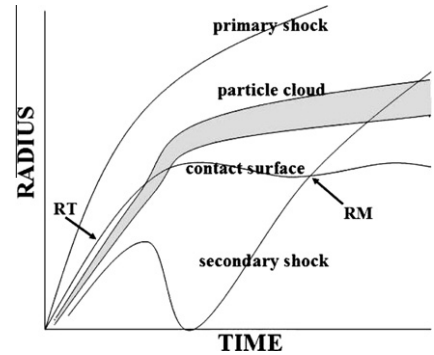

Fig. 1. x–t diagram showing the trajectories of the different waves. RT denotes Rayleigh–Taylor and RM denotes Richtmyer–Meshkov.

3. Results and discussion

We consider a 5.9 cm radius TNT charge with an ambient cloud of mono-disperse aluminum particles. A spherical sector grid spanning 2.4 m in length and 45° in the azimuth (θ) and zenith (ϕ) directions, is used with free-slip boundary conditions along the sides, and outflow in the outermost plane [7]. The TNT detonation products (C(S), H_2O, N_2, CO) are initialized within the initial charge radius with appropriate detonation profiles [7] and ambient air outside. Aluminum particles of 5 μm radius are randomly distributed in the region from outside the charge to a radial location of 8.68 cm, with $\eta = 1$ (η is the mass loading ratio, defined as the ratio of the mass of solid to gas in a given control volume). We considered 1000X45 X45 (G1), 1000X60X60 (G2), 1000X75X75 (G3) and 1000X90X90 (G4) grids, and our simulations show that whereas G1 barely suffices to capture the blast wave trajectory, overpressure, and ML boundaries, G2 is required to capture rms of velocity and concentration profiles in the ML, and also the particle clustering patterns' spatial widths. The finest grid, G4, produces nearly identical gas-phase profiles and particle cloud trajectories as G2 and G3. Thus, we employ G2 for this study. The trajectory and overpressure of the primary blast wave has been validated in [6,7]; there is, however, no known experimental data for the gas dynamics of the mixing layer behind explosions.

3.1. Dispersion and ignition

After the completion of detonation within the charge, a blast wave propagates outwards; the contact surface overtakes the particles and engulfs them (the first interaction event). An x–t diagram (schematic) of the primary shock, secondary shock, contact surface and particle cloud trajectories is presented in Fig. 1. The particles pick up momentum and energy from the gas—introducing perturbations on the contact surface during this interaction, which subsequently grows into Rayleigh–Taylor [4] instability. Ignition occurs in the cloud around $t/t_o \sim 5$ (t_o is the time required for detonation completion in the initial charge), initially at the leading edge since it is closer to the source of heat. Subsequently, the hydrodynamic structures decelerate more than the particles, as the latter have a higher inertia; this results in the leading edge (LE) of the particle cloud to interact with the hydrodynamic structures (the second interaction event). Around $t/t_o \sim 35$, the secondary shock (SS) implodes inward as the pressure has reduced considerably near the core due to the earlier rarefaction wave; the trailing edge (TE) of the particle cloud slows down as the local gas velocity reverses. At the same time, the LE of the cloud starts to emerge out of the hydrodynamic structures, and thus the choice of the oxidizer varies across the width of the particle cloud for the aluminum combustion: it is O_2 near the LE (aerobic); is H_2O near the TE (anaerobic); and a combination of multiple oxidizers (CO_2, H_2O, O_2) in the middle of the cloud that is currently in the ML. By this time, about 75% of the initial aluminum by mass has already evaporated, indicating that most of aluminum evaporation occurs primarily when the particles are engulfed inside the detonation products. Around the Rayleigh–Taylor structures, vortex rings exist due to shear and baroclinic effects; during the second interaction between the particles and the contact surface, these vortex rings manifest transverse velocities locally, causing the particles to also disperse in the transverse direction, giving rise to their clustering.

Subsequently, beyond $t/t_o \sim 75$, the particle cloud leaves the ML, and is quenched shortly due to the unavailability of heat in the relatively cooler surrounding air; analysis shows that only 12% of the original aluminum mass remains unevaporated for the chosen r_p and η. Once outside the ML, the particles disperse mostly along the radial direction, since vorticity effects are not as

significant outside the ML, and so the particle cloud maintains its clustered shape as it slows down due to aerodynamic drag. Meanwhile, the SS reflects from the origin ($t/t_o \sim 120$), subsequently explodes outwards and compresses the structures in the ML [6–8], giving rise to a Richtmyer–Meshkov instability [5]. Subsequently, around $t/t_o \sim 325$, the SS catches-up with the particle cloud and penetrates it, thereby shrinking the width of the cloud. However, the quenched particles do not re-ignite, as their interaction with the SS occurs radially far away where the latter has already attenuated by then.

3.2. Particle clustering

During the second interaction of the exploding particle cloud with the decelerating hydrodynamic structures, vorticity around the latter introduces transverse velocities to the particles. Since the particles are dispersing from the inner to the outer side of the ML, they interact first with the vortex rings around the bubbles. These vortex rings exist around the tip of the mushroom-like structures; in regions between contiguous structures where the fluid is primarily air only, vorticity is not as significant. This gives rise to preferential accumulation (or clustering) of particles, illustrated chronologically in Fig. 2 (the view presented is that as seen from the outermost plane of the sector looking inwards at the origin). At early times (Fig. 2(a)), the expanding particle cloud encounters the vortex rings and begins to also disperse in the transverse direction. Later, most of the transverse dispersion is complete, and the particles are clustered by $t/t_o \sim 45$ (Fig. 2(b)), and preserve their hydrodynamic foot print even after leaving the mixing layer (Fig. 2(c)). These clustering patterns are similar to the ones reported by Ling et al. [20] from a DNS study, albeit for planar mixing layers.

To better understand the actual clustering process, we consider four groups of particles based on their initial locations in the cloud: we denote as $C60$, a collection of 100 randomly chosen particles initially located at radial location $r = (6.0 \pm 0.1)$ cm; as $C70$, a collection of 100 randomly chosen particles initially located at radial location $r = (7.0 \pm 0.1)$ cm; similarly, $C80$ to $r = (8.0 \pm 0.1)$ cm; and $C86$ to $r = (8.6 \pm 0.1)$ cm. Specifically, we track the average particle velocities ($|u_\theta|, |u_\phi|$) of each group, and the average local gas velocity as seen by the particles corresponding to each group, presented in Fig. 3 (only u_θ is presented for brevity; the profiles are similar for u_ϕ). u_θ of each group of particles rises fast at early times, as they pick up momentum from the gas and are set into motion. Around $t/t_o \sim 20$, the particles start to interact with the vortex rings in the hydrodynamic structures, as evident from the peaks observed in Fig. 3(b). The transverse average local gas velocities around $t/t_o \sim 35$ are $\sim$20 m/s—this creates the transverse motion that results in the clustering around the hydrodynamic structures. Beyond $t/t_o \sim 60$, the average $|u_\theta|$ and $|u_\phi|$ of the particles and the local gas decrease rapidly, and asymptote to zero due to the absence of vorticity outside the ML.

3.3. Parametric study of particle clustering

3.3.1. Particle mass loading ratio

In addition to the above case, we also consider $\eta = 2$, for the same $r_p = 5$ μm and initial radial extent of the particle cloud distribution (5.9–8.68 cm). A higher η results in more perturbations on the contact surface during the first interaction event—consequently, more mixing and afterburn [7], later resulting in stronger/larger vortex rings around the Rayleigh–Taylor structures. The clustering for $\eta = 2$ is presented in Fig. 4(a); closer observation reveals that due to larger vortex rings, many clusters appear larger due to more transverse dispersion. To quantify this transverse motion, the average local gas transverse velocity as seen by particle group $C60$ is presented in Fig. 4(b) and, evidently, the gas transverse velocity components seen are slightly higher for the $\eta = 2$ case during the peak of the second interac-

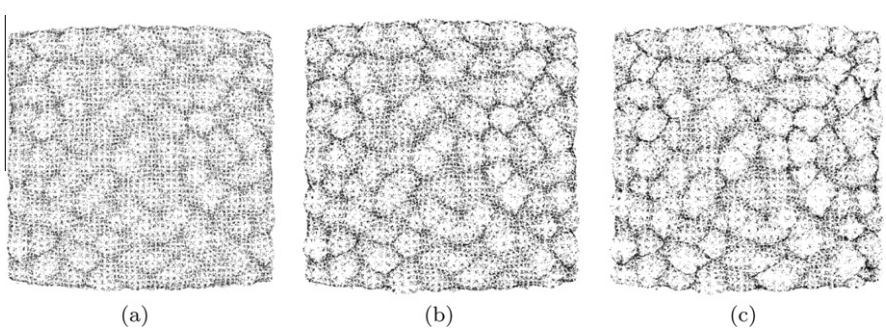

Fig. 2. Clustering of particle cloud at times (a) $t/t_o \sim 35$; (b) $t/t_o \sim 45$; and (c) $t/t_o \sim 90$. The scales of the figures have been adjusted for better clarity.

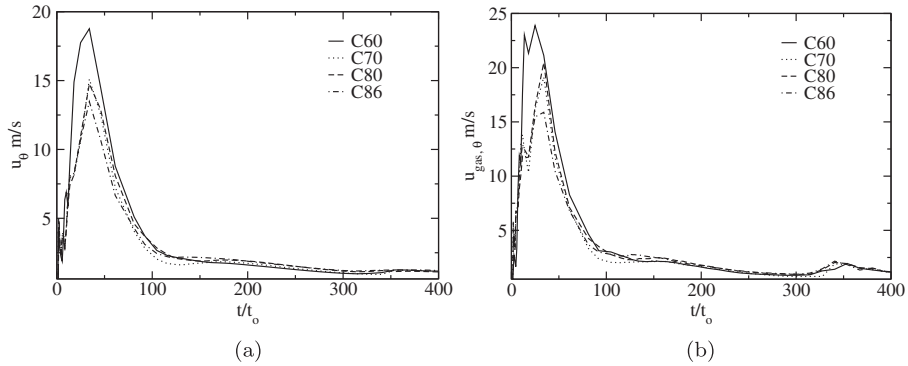

Fig. 3. Transverse velocities in the θ-direction: (a) average particle velocity and (b) average local gas velocity.

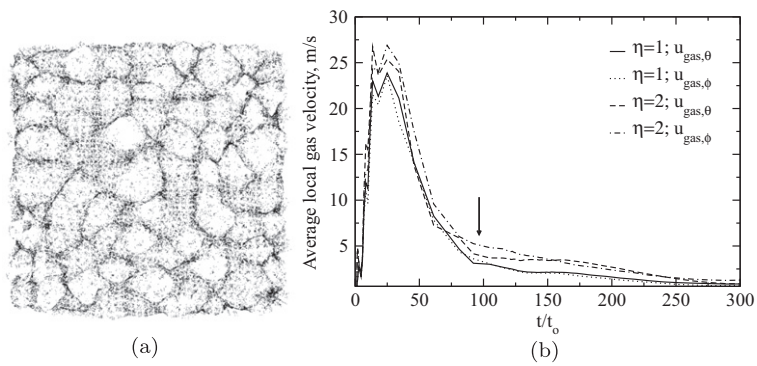

Fig. 4. Effect of η on clustering of particle cloud ($\eta = 2$): (a) clusters at $t/t_o \sim 90$ and (b) average local gas velocity seen by particle group $C60$.

tion ($t/t_o \sim 30$). Moreover, near the region indicated by the arrow, the gas transverse velocities are higher by a factor of 1.5–2—a direct consequence of more perturbations introduced to the contact surface by the $\eta = 2$ cloud, which enhances clustering of the particles.

3.3.2. Particle size and distribution

To investigate the effect of particle size on the clustering, we now consider $r_p = 10$ μm, with $\eta = 1$, and the cloud initially extending from $r = 5.9$–8.68 cm. Our analysis shows that this set up does not form clusters—for these 10 μm radius particles, ignition is delayed *vis-à-vis* the 5 μm radius particles, due to which they are still sufficiently large (~8–8.5 μm radius) during the second interaction event. In comparison, the particles in the 5 μm cloud easily ignite during their engulfment into the detonation products, and are about 2.5–3 μm in radius during the second interaction event; here, particle size during the second interaction event decides whether or not clustering will occur, as the inter-phase momentum transfer time scales as r_p^2. On the other hand, by considering 10 μm radius particle clouds corresponding to $\eta = 1$, but an initial distribution extending from $r = 5.9$–12 cm, clustering is observed and is presented in Fig. 5(a). A *prima facie* observation is that fewer clusters are observed in Fig. 5(a) compared to Fig. 2, and are also more degenerate due to the larger particle size having larger momentum transfer time scales. This study illustrates that while a threshold particle size for the formation of clusters may not be relevant, the particle size that can result in clustering depends on the initial width of the cloud, and presumably, also on the initial charge size and choice of the high explosive. Moreover, the transition from 'clustering' to 'no-clustering' events is gradual, and so the definition of what constitutes a cluster is rather *ad hoc*. Thus, no attempt is made to ascertain a threshold particle size for cluster formation.

In Fig. 5(b), the average local gas transverse ($u_{gas,\theta}, u_{gas,\phi}$) velocities as seen by the particle group $C60$ for $r_p = 10$ μm, $\eta = 1$, and the initial particle cloud extending radially from $r = 5.9$–8.68 cm and $r = 5.9$–12 cm, are presented. As evident, the transverse gas velocities seen by the particles are higher, when the initial cloud width is wider and, consequently, the clustering is more pronounced

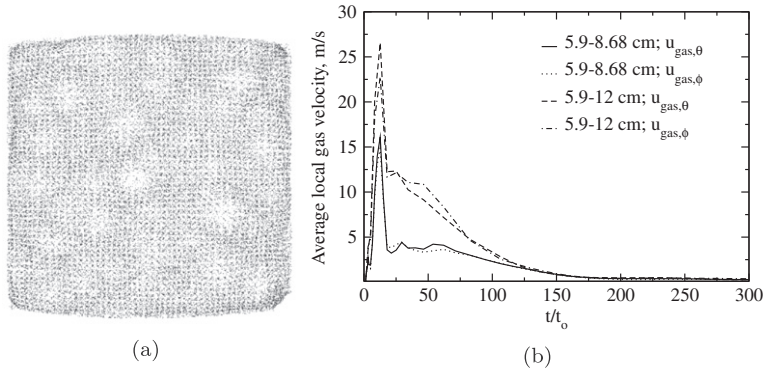

Fig. 5. Effect of particle size on clustering of particle cloud ($r_p = 10$ μm; initial cloud distribution: 5.9–12 cm; $\eta = 1$): (a) clusters at $t/t_o \sim 90$ and (b) average local gas velocity seen by particle group $C60$.

(similar comments hold for the other particle groups, $C70$, etc.).

3.3.3. Relevant time scales

The time scales of the particles are estimated based on their respective size and the local gas properties during the second interaction event, and are presented in Table 1. Here, the vortex residence time denotes the approximate time a particle resides in the vortex rings. Both particles have burn times larger than the vortex residence times—so they do not completely burn during their interaction with the vortex rings. For the 5 μm particles, the momentum and heat transfer time scales are significantly smaller than the vortex time; thus, clustering occurs and, in addition, also preferential particle heating (shown below). However, for the 10 μm particles, the momentum and heat transfer time scales are comparable to the vortex residence times; thus, they are less prone to transverse dispersion and clustering.

3.4. Aluminum combustion

After the particles ignite during their early engulfment into the detonation products, their sustenance of burning depends on the clustering aspects, due to which preferential combustion of particles occurs subsequently. Particles accumulated in the afterburning regions around the hydrodynamic structures can burn longer than those in the surrounding regions owing to the availability of the afterburn energy, and is illustrated in Fig. 6, corresponding to $r_p = 5$ μm, $\eta = 1$, and the initial cloud extending from $r = 5.9$–8.68 cm. From Fig. 6(a), significant particle temperature gradients are observed to exist during this burning phase, as evident from the transitions between the red and the green regions[1]; this corresponds to the time instant when the particles are interacting with the hydrodynamic structures in the ML; later (Fig. 6(b)) the particles quench and have clustered around the hydrodynamic structures. The white regions in (b) denote particle-free regions, demonstrating significant transverse dispersion of particles upon interaction with the vortex rings in the ML.

The exact amount of formation of aluminum oxides can be quantified by investigating the instantaneous total mass of AlO and $Al_2O_3(L)$, and is presented in Fig. 7, normalized with the initial mass of solid aluminum; the cases presented here correspond to the initial cloud width from $r = 5.9$–8.68 cm. Once the particles are engulfed inside the detonation products, since ignition occurs earlier for aluminum particles of size $r_p = 5$ μm than 10 μm, the AlO mass starts to rise earlier for the former. Around $t/t_o \sim 15$, $Al_2O_3(L)$ starts to rise—this being the time instant when the leading edge of the particle cloud enters the ML—where both aerobic and anaerobic combustion concurrently occur. Due to the relatively delayed ignition of the 10 μm radius particles, they undergo a higher proportion of aerobic burning as evident from the earlier rise of the $Al_2O_3(L)$ mass. At late times, the mass of AlO and $Al_2O_3(L)$ asymptotes, as the particles quench after they leave the ML. In summary, aluminum burning is anaerobic initially; both aerobic and anaerobic burning co-exist at intermediate times when

Table 1
Relevant approximate time scales (in μs) for 5 and 10 μm radius particles.

Time scale	5 μm	10 μm
Burn time [12]	1000	2000
Momentum transfer	40	160
Heat transfer	40	200
Vortex residence	200–300	200–300

[1] For interpretation of color in Fig. 6, the reader is referred to the web version of this article.

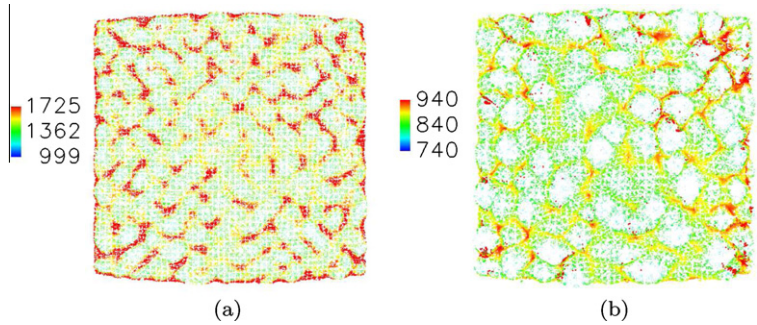

Fig. 6. Preferential combustion of aluminum particles: particle temperature (in K) at times (a) $t/t_o \sim 25$ and (b) $t/t_o \sim 120$.

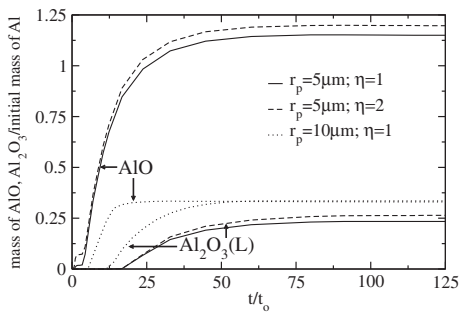

Fig. 7. Products of aluminum combustion: instantaneous total mass of aluminum oxides normalized with the initial mass of solid aluminum.

the particles traverse the ML; and, later, burning is strictly aerobic outside the ML; finally, the particles quench and the aluminum products mass asymptotes.

3.5. Theoretical considerations

Many theoretical models have been used in the past to model the growth of hydrodynamic instabilities in classical gravity-driven fluid interfaces as well as blast wave driven systems; among these, the Buoyancy–Drag (BD) model is common [21–23]. Here, the rise of bubbles is modeled accounting for buoyancy, drag and decompression effects. The bubble amplitude (h) is obtained as [21]

$$\frac{d}{dt}\frac{dh(t)}{dt} = \widetilde{A}g(t) - \frac{\widetilde{C}}{\lambda}u_{inst}(t)^2 + \frac{d}{dt}\omega(t)h(t), \qquad (3)$$

where $\widetilde{A}$ denotes the postshock-modified Atwood number, $g(t)$ is the driving acceleration, $\widetilde{C}$ is the modified drag coefficient, λ is the perturbation wavelength, u_{inst} is the instability velocity (i.e., how fast the perturbation grows away from the unperturbed interface), and $\omega(t)$ is the radial velocity gradient evaluated at the interface. Following [21], the amplitude is obtained as $\frac{dh}{dt} = u_{inst}(t) + \omega(t)h(t)$, and substituting this into Eq. (3), we obtain the standard BD equation $\frac{du_{inst}}{dt} = Ag(t) - \frac{C}{\lambda}u_{inst}(t)^2$. Based on the simulation for the $r_p = 5$ μm, $\eta = 1$ case, we consider an ensemble of 10 bubbles, and measure their amplitude (h) and transverse scale (L) at different times. In addition, a single-phase, unperturbed 1D simulation is carried out to obtain the interface radius, $r_i(t)$, and is used to obtain $g(t)$ and $\omega(t)$. The $L(t)$ for the bubble ensemble from the simulation are used to compute $u_{inst}(t)$, and from it $h(t)$ is evaluated. Self-similarity of bubbles at late times is of interest, and is a debated topic in recent literature [21], albeit not previously studied for chemical explosions. Here, self-similarity refers to the growth of bubble amplitudes (h) proportional to their transverse scale (L). This analysis is performed using the initial amplitudes from $t/t_o \sim 12$—approximately the time required for the contact surface to overtake the initial particle cloud, until $t/t_o \sim 160$—the time when the secondary shock explodes into the ML during the reshock phase.

Analysis shows that a range of length scales exist for the bubbles, as shown in Fig. 8(a), including some "runaways" [24]. We classify the bubbles into three branches—lower, middle and upper, and use three $L(t)$ curve-fits for the current analysis (length scales are normalized with the initial charge radius, r_o). The L/h ratio for the bubbles from the 3D simulation is shown in Fig. 8(b), and suggests $L/h \sim 0.5$–1.1 at early times, but tends to asymptote near $t/t_o \sim 150$ to 0.2 ± 0.07; this evidences that self-similar growth of the bubbles is possible at late times. The runaway bubbles shown do not conform to self-similarity. The definition of λ is critical to the BD model analysis. Some researchers have used $\lambda = L$ [22], while others have used $\lambda = 2L$ [23] (ideally, λ should be the volume to cross-sectional area ratio for the bubbles). We make both considerations in our analysis, and present in Fig. 9 the bubble amplitude (h) obtained from the BD model for the lower, middle and upper branches, for both λ definitions. As evident, with $\lambda = 2L$, the h predicted by the BD

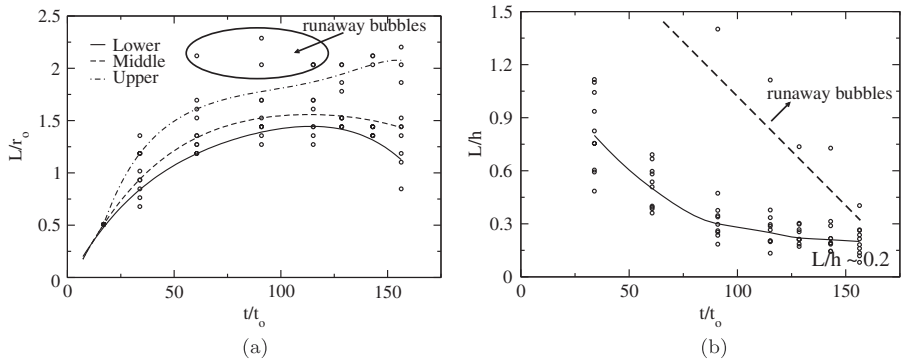

Fig. 8. Bubble dynamics from the 3D simulation: (a) L and (b) L/h. The circles denote the 3D simulation results.

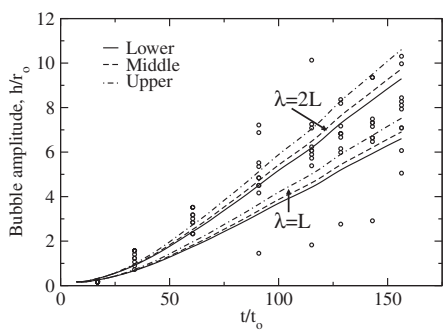

Fig. 9. Bubble amplitudes obtained from the BD model. The circles denote the 3D simulation results.

model is in better qualitative agreement with the simulation results for large amplitude bubbles; with $\lambda = L$, the BD model predicts h that conforms better to the simulation results for small amplitude bubbles. This clearly demonstrates that large transverse scale (L) bubbles (smaller volume to cross-sectional area ratio) have smaller amplitudes (h), and vice versa. Larger transverse scale bubbles have larger frontal area and are thus slowed down easily by aerodynamic drag, unlike smaller transverse scale bubbles that can rise farther before drag effects come into play. Indeed, our simulation results show that during the implosion phase, small bubbles, albeit not all, implode deep into the core—thereby increasing their amplitude. These bubbles are more elongated in shape and have a higher volume-to-area ratio; thus, it is not surprising that the BD model predicts a higher amplitude for $\lambda = 2L$.

4. Conclusions

A robust hybrid two-phase numerical methodology is used to study the flow-field subsequent to the detonation of an explosive charge surrounded by an ambient dilute cloud of solid particles. Rayleigh–Taylor instability is observed at the contact surface that separates the inner detonation products and the outer air, which subsequently results in a mixing layer where they afterburn. At early times, the particles are engulfed into the detonation products completely, where they pick up heat and ignite; pick up momentum and disperse. Subsequently, as the particles disperse outwards, they interact with the vortex rings around the hydrodynamic structures, which introduces transverse dispersion and clustering. Preferential particle heating and combustion are observed in the cloud, with particles in the afterburning regions burning more than their counterparts. With twice the initial mass loading in the ambient cloud, slightly larger clusters are observed, due to stronger/larger vortex rings around the hydrodynamic structures owing to more particles available to perturb the contact surface during the first interaction. For a larger particle radius cloud, clustering is not observed for the same initial radial cloud width; however, when present in a wider initial cloud, fewer and degenerate clusters form, indicating that particle size during the second interaction event is critical to the clustering process. Furthermore, the bubbles are observed to attain self-similar growth at the later stages of the explosion. A theoretical Buoyancy–Drag model is used to evaluate the bubble amplitudes, and the predictions are in qualitative accordance with the simulation results.

Acknowledgments

This research work was supported in part by the Office of Naval Research (Dr. Cliff Bedford, Program Manager) and the Air Force Research Laboratory, Eglin Air Force Base (Dr. Douglas Nance, Program Manager). Simulations were carried out at the DoD High Performance Computing Centers at Army Research Laboratory

DSRC and Maui High Performance Computing Center DSRC.

References

[1] A.L. Kuhl, P. Neuwald, H. Reichenbach, *Combust. Expl. Shock Waves* 42 (6) (2006) 731–734.
[2] A.L. Kuhl, H. Reichenbach, *Proc. Combust. Inst.* 32 (2009) 2291–2298.
[3] F. Zhang, J. Anderson, A. Yoshinaka, *CP955 Shock Compression of Condensed Matter*, AIP, 2007.
[4] G.I. Taylor, *Proc. Royal Soc. Lond. A, Math. Phys. Sci.* 201 (1950) 192–196.
[5] R.D. Richtmyer, *Commun. Pure Appl. Math.* 13 (1960) 297–319.
[6] K. Balakrishnan, F. Genin, D.V. Nance, S. Menon, *Shock Waves* 20 (2) (2010) 147–162.
[7] K. Balakrishnan, S. Menon, *Combust. Sci. Technol.* 182 (2) (2010) 186–214.
[8] A.L. Kuhl, *Dynamics of Exothermicity*, Gordon and Breach Publishers, 1996, p. 291.
[9] E. Leinov, G. Malamud, Y. Elbaz, et al., *J. Fluid Mech.* 626 (2009) 449–475.
[10] A.R. Miles, *Phys. Plasmas* 11 (11) (2004) 5140–5155.
[11] A.R. Miles et al., *Phys. Plasmas* 12 (5) (2005) 056317.
[12] V. Tanguay, S. Goroshin, A.J. Higgins, F. Zhang, *Combust. Sci. Technol.* 181 (4) (2009) 670–693.
[13] T. Bazyn, H. Krier, N. Glumac, *Proc. Combust. Inst.* 31 (2) (2007) 2021–2028.
[14] F. Genin, S. Menon, *J. Turbul.* 11 (4) (2010) 1–30.
[15] F. Genin, S. Menon, *Comput. Fluids* 39 (5) (2010) 800–819.
[16] S. Menon, N. Patel, *AIAA J.* 44 (4) (2006) 709–723.
[17] S. Xu, D.S. Stewart, *J. Eng. Math.* 31 (2–3) (1997) 143–172.
[18] E.F. Toro, *Riemann Solvers and Numerical Methods for Fluid Dynamics*, Springer, 1999.
[19] A. Khasainov, B. Veyssiere, *Prog. Astro. Aero.* 114 (1988) 284–299.
[20] W. Ling, J.N. Chung, T.R. Troutt, C.T. Crowe, *J. Fluid Mech.* 358 (1998) 61–85.
[21] A.R. Miles, *Astrophys. J.* 696 (2009) 498–514.
[22] G. Dimonte, M. Schneider, *Phys. Rev. E* 54 (1996) 3740.
[23] D. Oron, L. Arazi, D. Kartoon, A. Rikanati, U. Alon, D. Shvarts, *Phys. Plasmas* 8 (2001) 2883.
[24] J. Glimm, O. McBryan, R. Menikoff, D.H. Sharp, *Phys. Lett. A* 123 (6) (1987) 289–292.